PAPER • OPEN ACCESS

Calculation and measurement of coupling loss in a no-insulation *Re*BCO racetrack coil exposed to AC magnetic field

To cite this article: Simon Otten *et al* 2023 *Supercond. Sci. Technol.* **36** 044002

View the article online for updates and enhancements.

Calculation and measurement of coupling loss in a no-insulation *Re*BCO racetrack coil exposed to AC magnetic field

Simon Otten*[iD], Jeroen ter Harmsel[iD], Marc Dhallé and Herman Ten Kate[iD]

Faculty of Science and Technology, University of Twente, Drienerlolaan 5, Enschede,7522NB, The Netherlands

E-mail: s.j.otten@utwente.nl

CrossMark

Abstract

No-insulation coils are self-protecting and can therefore generally be operated at higher current densities. However, the electrical turn-to-turn connections may cause additional AC loss when charging the coil or when it is exposed to a time-dependent magnetic field. In this work, we study the case of a no-insulation *Re*BCO tape racetrack coil exposed to a uniform AC field applied parallel to the tape surface. We show that an anisotropic continuum model allows to formulate analytical approximations for coupling loss in the low- and high-frequency limits. For intermediate frequencies, the continuum model needs to be evaluated numerically. The model was validated with representative measurements of AC loss in the coils, measured calorimetrically as well as magnetically using pick-up coils. The validation experiment confirms the predicted frequency dependence of the coupling loss, which is $P \propto f^2$ at low frequencies and $P \propto \sqrt{f}$ at high frequencies, due to the skin effect. The transition between low- and high-frequency regimes occurs around a characteristic frequency f_c that is directly related to the characteristic time constant $\tau = 1/2\pi f_c$ associated with the current decay in (dis)charge experiments.

Keywords: AC loss, no-insulation coil, *Re*BCO

(Some figures may appear in colour only in the online journal)

1. Introduction

In 2011, Hahn *et al* proposed *Re*BCO tape coils without turn-to-turn insulation for application in a 1.3 GHz nuclear magnetic resonance (NMR) magnet. A higher current density, better mechanical integrity and thermal stability were mentioned as potential advantages over insulated coils [1]. Since then, no-insulation *Re*BCO coils have been successfully applied in a number of high-field magnets [2–4]. No-insulation coils are also considered for application in rotating machines [5–14] and in linear actuators [15–17]. However, in such devices the coils are subjected to time-dependent magnetic fields and may well suffer from additional coupling loss due to induced currents that flow through the turn-to-turn contacts, as recently illustrated by Wang *et al* in no-insulation round pancake-type coils [18]. These coupling losses are specifically addressed in this article. For the design of AC devices based on no-insulation coils, it is useful to develop and verify theories that efficiently but accurately predict such

---

coupling loss, so that it can be compared against other loss components.

The temporal variation of the magnetic field generated by the coils themselves was investigated in a number of studies, although AC loss was not analyzed in detail [7, 19–23]. Kim *et al* measured the AC loss with an applied AC current [24] and found that the no-insulation coils had lower AC loss than their insulated counterparts because the turn-to-turn contacts create a bypass for the applied current. However, Wang *et al* observed 10 to 20 times higher AC loss in a no-insulation coil compared to a similar coil with turn-to-turn insulation in an applied magnetic field of 70 Hz [18]. A numerical calculation showed that the induced currents flow largely in the outer turns due to the skin effect.

In this work, the coupling loss in a no-insulation racetrack coil placed in a uniform AC field perpendicular to the plane of the coil is studied. Although non-uniform magnetic fields and higher harmonics are expected in real AC devices, only a uniform sinusoidal magnetic field will be considered for now. We use a model in which the no-insulation coil is represented by a uniform material with anisotropic resistivity, an approach first presented by Mataira *et al* [25]. The simplicity of the model enables one to find analytical solutions for a few limiting cases. Such analytical estimates for the coupling loss in the high- and low-frequency limits are presented in sections 3.1 and 3.2, respectively. In order to verify the calculations, a set of dedicated small racetrack coils with soldered turns was constructed. The coils are mounted inside a wide-bore dipole magnet, which can apply a uniform AC magnetic field. The AC loss in the racetrack coils is measured magnetically as well as calorimetrically.

2. Continuum model for current distribution

We use a continuum model to calculate the current distribution in the racetrack coil. This model represents the coil as a homogeneous material with an anisotropic resistivity. Such a model was first proposed for pancake coils by Mataira *et al* [25] and has also been used to describe AC loss in Roebel cables [26]. An advantage is that the three-dimensional coil geometry can be reduced to two dimensions, thereby reducing computation time. In addition, it is possible to find analytical solutions that can provide a quick estimate of coupling loss in a few limiting cases.

In this section, the anisotropic $\mathbf{E}(\mathbf{J})$ relation is first derived for a pancake coil and then modified for racetrack-type coils.

The homogenization procedure is illustrated for a round coil in figure 1. The pancake-type coil has N turns of thickness d, an inner and outer radius of r_1 and r_2, respectively, and an axial 'height' (the tape width) of h. The turns are separated by a resistive barrier with a surface resistivity R_{ct}, with unit Ωm^2. The radial position of the conductor increases by d after every full turn. The angle α between the conductor and the azimuthal θ-direction (figure 1) is therefore given by:

$$\tan(\alpha) = \frac{d}{\ell_{turn}} = \frac{d}{2\pi r}.$$ (1)

The homogenized coil has a resistivity $\rho_\perp$ perpendicular—and $\rho_\parallel$ parallel to the conductor. Neglecting the internal transverse resistance of the conductor [27], the perpendicular resistivity is related to the inter-turn contact resistivity by $\rho_\perp = R_{ct}/d$. The parallel resistivity $\rho_\parallel$ is determined by the longitudinal resistance of the conductor and can be described using Ohm's law for metal wires and a non-linear power-law for superconducting wires. The applied current enters the coil at the inner radius $r = r_1$ and exits at $r = r_2$. Assuming a homogeneous current injection and extraction over the available inner and outer surface, the applied radial current density is $J_{a,1}(t) = I_a(t)/2\pi r_1 h$ at the inner radius and $J_{a,2}(t) = I_a(t)/2\pi r_2 h$ at the outer radius.

The electric field components perpendicular and parallel to the conductor in the homogenized coil are given by:

$$\begin{bmatrix} E_\perp \\ E_\parallel \end{bmatrix} = \begin{bmatrix} \rho_\perp & 0 \\ 0 & \rho_\parallel \end{bmatrix} \begin{bmatrix} J_\perp \\ J_\parallel \end{bmatrix}.$$ (2)

As indicated in figure 1, the current densities $(J_\perp, J_\parallel)$ in the frame of the conductor can be related to the polar current densities J_r and J_θ by clockwise rotation with an angle α:

$$\begin{bmatrix} J_\perp \\ J_\parallel \end{bmatrix} = \begin{bmatrix} \cos(\alpha) & -\sin(\alpha) \\ \sin(\alpha) & \cos(\alpha) \end{bmatrix} \begin{bmatrix} J_r \\ J_\theta \end{bmatrix}.$$ (3)

In the same way, the electric fields (E_r, E_θ) in the polar coordinate system are found by a counter-clockwise rotation of the electric field $(E_\perp, E_\parallel)$ in the frame of the conductor:

$$\begin{bmatrix} E_r \\ E_\theta \end{bmatrix} = \begin{bmatrix} \cos(\alpha) & \sin(\alpha) \\ -\sin(\alpha) & \cos(\alpha) \end{bmatrix} \begin{bmatrix} E_\perp \\ E_\parallel \end{bmatrix}.$$ (4)

An $\mathbf{E}(\mathbf{J})$ relation in polar coordinates can be found by substitution of equations (2) and (3) into (4):

$$\begin{aligned} \begin{bmatrix} E_r \\ E_\theta \end{bmatrix} &= \begin{bmatrix} \cos(\alpha) & \sin(\alpha) \\ -\sin(\alpha) & \cos(\alpha) \end{bmatrix} \begin{bmatrix} \rho_\perp & 0 \\ 0 & \rho_\parallel \end{bmatrix} \begin{bmatrix} \cos(\alpha) & -\sin(\alpha) \\ \sin(\alpha) & \cos(\alpha) \end{bmatrix} \begin{bmatrix} J_r \\ J_\theta \end{bmatrix} \\ &= \begin{bmatrix} \rho_\perp \cos^2(\alpha) + \rho_\parallel \sin^2(\alpha) & (\rho_\parallel - \rho_\perp)\sin(\alpha)\cos(\alpha) \\ (\rho_\parallel - \rho_\perp)\sin(\alpha)\cos(\alpha) & \rho_\parallel \cos^2(\alpha) + \rho_\perp \sin^2(\alpha) \end{bmatrix} \begin{bmatrix} J_r \\ J_\theta \end{bmatrix}. \end{aligned}$$ (5)
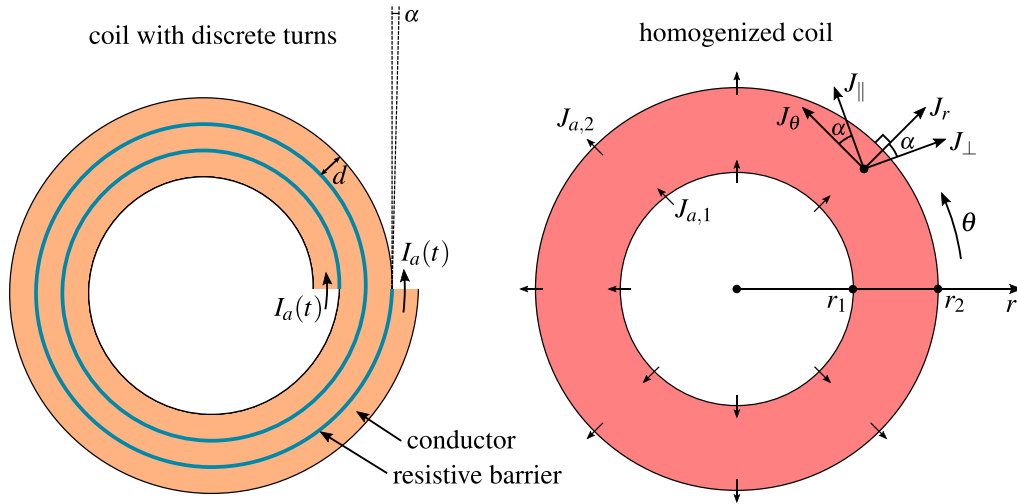
Figure 1. Approximation of a round pancake-type coil by a homogeneous short hollow cylinder with an anisotropic resistivity.
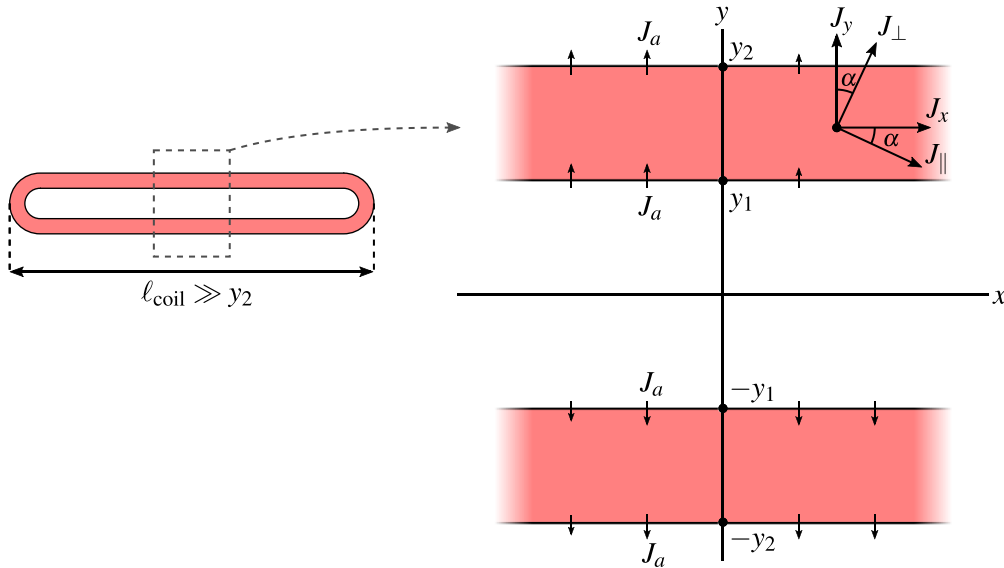

Figure 2. The continuum model for a long racetrack coil.

Note that after homogenization, the coil becomes axisymmetric. The spiraling shape of the conductor is captured with the anisotropic resistivity. As long as the external field is axisymmetric as well, the problem can thus be solved in two dimensions, greatly reducing computation time.

The above equations are valid for a cylindrical coil. The derivation for an elongated racetrack coil (figure 2) is very similar and can be found by exchanging θ and r with the Cartesian coordinates x and y, respectively. This results in the following relations:

$$\begin{bmatrix} J_\parallel \\ J_\perp \end{bmatrix} = \begin{bmatrix} \cos(\alpha) & -\sin(\alpha) \\ \sin(\alpha) & \cos(\alpha) \end{bmatrix} \begin{bmatrix} J_x \\ J_y \end{bmatrix} \tag{6}$$

$$\begin{bmatrix} E_x \\ E_y \end{bmatrix} = \begin{bmatrix} \cos(\alpha) & \sin(\alpha) \\ -\sin(\alpha) & \cos(\alpha) \end{bmatrix} \begin{bmatrix} E_\parallel \\ E_\perp \end{bmatrix} \tag{7}$$

$$\begin{aligned} \begin{bmatrix} E_x \\ E_y \end{bmatrix} &= \begin{bmatrix} \cos(\alpha) & \sin(\alpha) \\ -\sin(\alpha) & \cos(\alpha) \end{bmatrix} \begin{bmatrix} \rho_\parallel & 0 \\ 0 & \rho_\perp \end{bmatrix} \begin{bmatrix} \cos(\alpha) & -\sin(\alpha) \\ \sin(\alpha) & \cos(\alpha) \end{bmatrix} \begin{bmatrix} J_x \\ J_y \end{bmatrix} \\ &= \begin{bmatrix} \rho_\parallel \cos^2(\alpha) + \rho_\perp \sin^2(\alpha) & (\rho_\perp - \rho_\parallel)\sin(\alpha)\cos(\alpha) \\ (\rho_\perp - \rho_\parallel)\sin(\alpha)\cos(\alpha) & \rho_\perp \cos^2(\alpha) + \rho_\parallel \sin^2(\alpha) \end{bmatrix} \begin{bmatrix} J_x \\ J_y \end{bmatrix}. \end{aligned} \tag{8}$$

The tangent of the angle between the conductor and the *x*-axis equals the ratio of the conductor thickness and turn length. For a long racetrack coil, the length of each turn is approximately equal to twice the length of the coil:

$$\tan(\alpha) = \frac{d}{\ell_{\text{turn}}} \approx \frac{d}{2\ell_{\text{coil}}}. \tag{9}$$

3. Analytical solutions of the continuum model

Although a general solution of the continuum model requires numerical evaluation, analytical expressions can be derived for certain limiting cases. Here, the coupling loss will be calculated for a long racetrack coil exposed to a uniform harmonically varying external magnetic field applied in the vertical direction (*z*) (see figure 3). It is assumed that the turns have an infinite critical current density ($\rho_\parallel = 0$) and that the induced current only flows in the *x*-direction. Under these assumptions the relation between electric field and current density (equation (8)) reduces to:

$$E_x = \rho_\perp \sin^2(\alpha) J_x. \tag{10}$$

3.1. Solution in the low-frequency limit

Applying a uniform AC field to a no-insulation coil caused induced currents with a characteristic time constant τ, which is determined by the inductance and the resistance of the current path. In the low-frequency limit, it is assumed that the external magnetic field changes slowly compared to this time constant, i.e. $\omega \ll 1/\tau$:

$$B_z \approx B_0 \sin(\omega t). \tag{11}$$

The electric field follows from Faraday's law:

$$\frac{\partial E_x}{\partial y} = \frac{\partial B_z}{\partial t} \quad \Rightarrow \quad E_x = B_0 \omega \cos(\omega t) y + C. \tag{12}$$

Choosing $y = 0$ in the center of the coil and invoking symmetry, the integration constant C is set to zero so that the electric field and current density are odd functions of *y*. The current density can then be computed from equation (10) as:

$$J_x = \frac{E_x}{\rho_\perp \sin^2(\alpha)} = \frac{B_0 \omega \cos(\omega t) y}{\rho_\perp \sin^2(\alpha)}. \tag{13}$$

The AC loss per cycle can now be found by integration of $E_x J_x$ over the cross-sectional area of the coil and a full cycle of the magnetic field:

$$\frac{Q}{\ell h} = \frac{2 B_0^2 \omega^2}{\rho_\perp \sin^2(\alpha)} \int_0^{\frac{2\pi}{\omega}} \cos^2(\omega t) \mathrm{d}t \int_{y_1}^{y_2} y^2 \mathrm{d}y$$

$$= \frac{2\pi B_0^2 \omega (y_2^3 - y_1^3)}{3 \rho_\perp \sin^2(\alpha)}. \tag{14}$$

This equation gives the loss per unit length ℓ and height *h*. The factor 2 is introduced to account for both coil halves.

3.2. Solution in the high-frequency limit

If the applied magnetic field changes fast compared to the characteristic time constant ($\omega \gg 1/\tau$), the influence of induced currents on the magnetic field can no longer be neglected. The applied field will only penetrate in a skin near the outer surface, and the induced currents in this skin will shield the inner part of the coil. Here, the problem in this high-frequency limit is solved in two steps. First, the magnetic field on the surface of the coil is calculated assuming full expulsion of the magnetic field. Then, the magnetic field near surface will be computed by solving the 1D magnetic diffusion equation in order to estimate the coupling loss.

As schematically indicated in figure 4, expulsion of the magnetic field leads to a higher effective magnetic field B_{eff} on the surface. The enhancement factor $1/(1 - N) = B_{\text{eff}}/B_0$, with N the demagnetization factor of the coil leg [28], depends on the aspect ratio of the coil. For typical racetrack coils that are wider than they are tall ($2y_2 \gg h$), this factor cannot be neglected. In the appendix we propose a way to compute *N* from the aspect ratio using conformal mapping. Alternatively, it can also be found numerically, by solving $\nabla \times \mathbf{B} = 0$ in the area outside of the coil [29–31].

Once the effective magnetic field B_{eff} is known we can compute the induced current near the surface in order to find the coupling loss. Assuming current in the *x*-direction and magnetic field in the *z*-direction only, the laws of Ampère and Faraday become:

$$\frac{\partial B_z}{\partial y} = \mu_0 J_x \tag{15}$$

$$\frac{\partial E_x}{\partial y} = \frac{\partial B_z}{\partial t}. \tag{16}$$

With equation (10), we now have three equations with three unknowns (J_x, E_x and B_z) fully describing the current distribution in the coil.

Elimination of J_x and E_x gives the following 1D diffusion equation for the magnetic field:

$$\frac{\partial B_z}{\partial t} = \eta \frac{\partial^2 B_z}{\partial y^2}, \tag{17}$$

where η is a diffusion constant given by:

$$\eta = \frac{\rho_\perp \sin^2(\alpha)}{\mu_0}. \tag{18}$$

The solution that satisfies the boundary conditions $B_z(-\infty, t) = 0$ and $B_z(y_2, t) = B_{\text{eff}} \sin(\omega t)$ is given by:

$$B_z(y, t) = B_{\text{eff}} \, e^{\frac{y - y_2}{\delta}} \sin(\omega t + \frac{y - y_2}{\delta}), \tag{19}$$

where

$$\delta = \sqrt{\frac{2\eta}{\omega}} = \sqrt{\frac{2 \rho_\perp \sin^2(\alpha)}{\mu_0 \omega}}. \tag{20}$$
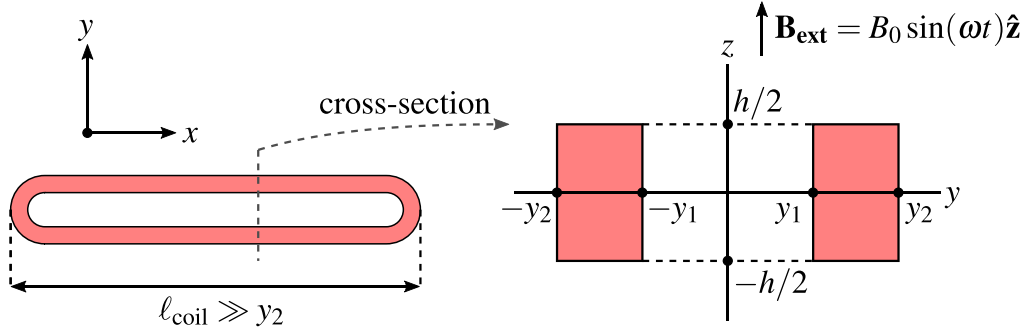
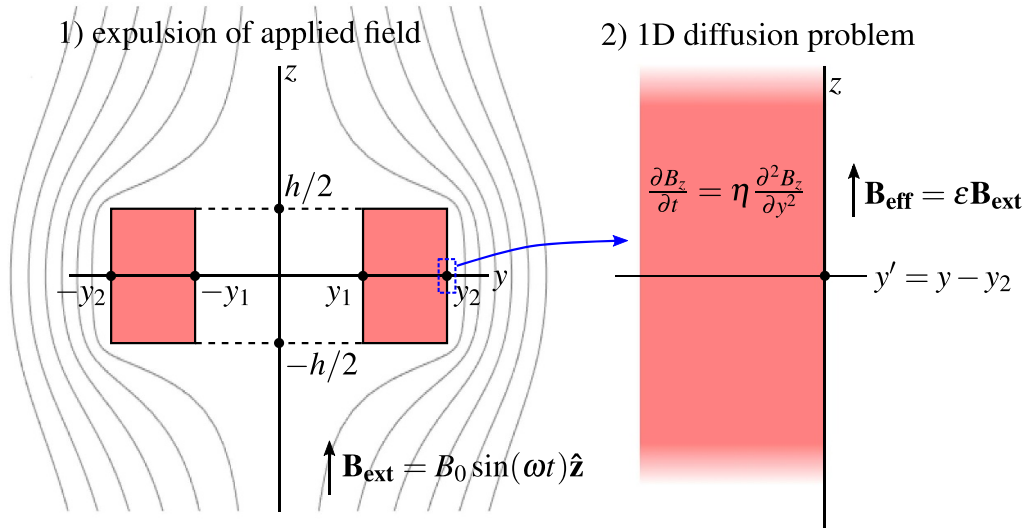**Figure 3.** Long racetrack coil of finite height h.

Figure 4. Approach for computing the coupling loss in the high-frequency limit. First the magnetic field on the surface assuming perfect diamagnetism is calculated. Then the diffusion problem is solved near the surface.

The constant δ is the characteristic length scale over which the magnetic field attenuates from the outer surface of the coil (the skin depth). A plot of the solution is shown in figure 5. The current density follows from Ampere's law (equation (15)):

$$J_x(y,t) = \frac{1}{\mu_0}\frac{\partial B_z}{\partial y} = \frac{B_{\text{eff}}}{\mu_0 \delta} e^{\frac{y-y_2}{\delta}} \left(\sin\left(\omega t + \frac{y-y_2}{\delta}\right) \right. $$
$$\left. + \cos\left(\omega t + \frac{y-y_2}{\delta}\right) \right) \quad (21)$$

The energy flux into the coil can be found by evaluating the Poynting vector $\mathbf{S} = \mu_0^{-1}\mathbf{E} \times \mathbf{B}$ on the surface.

$$S_y(y_2,t) = -\frac{E_x(y_2,t)B_z(y_2,t)}{\mu_0} = -\frac{B_{\text{eff}}^2 \rho_\perp \sin^2(\alpha)}{\mu_0^2 \delta}(\sin^2(\omega t) $$
$$+ \sin(\omega t)\cos(\omega t)). \quad (22)$$

Finally, the coupling loss per cycle is computed by multiplying this with the area $2\ell_{\text{coil}}h$ exposed to the applied field and integrating over a full cycle:

$$Q = -2\ell_{\text{coil}}h \int_0^{\frac{2\pi}{\omega}} S_y(y_2,t)\mathrm{d}t = 2\ell_{\text{coil}}h\frac{B_{\text{eff}}^2 \rho_\perp \sin^2(\alpha)}{\mu_0^2 \omega \delta}. \quad (23)$$

Using equation (20) for the skin depth, this can be simplified to:

$$\frac{Q}{\ell_{\text{coil}}h} = \frac{\pi B_{\text{eff}}^2 \delta}{\mu_0}. \quad (24)$$

4. Numerical solution of the continuum model

To compute the coupling loss at intermediate frequencies, the model is solved numerically. The numerical method also makes it possible to use a power-law type of resistivity in the direction parallel to the conductor:

$$\rho_\parallel = \frac{E_c}{|J_\parallel|}\left|\frac{J_\parallel}{J_c}\right|^n. \quad (25)$$

To find a numerical solution, the cross-sectional area is divided in rectangles with uniform current density. A method proposed by Brandt *et al* [32, 33] is used to find a system of ordinary differential equations that describes the current densities. The application of this method is described in detail in a publication about *Re*BCO Roebel cables [26], which in the cross-section also appear as two side-by-side stacks of
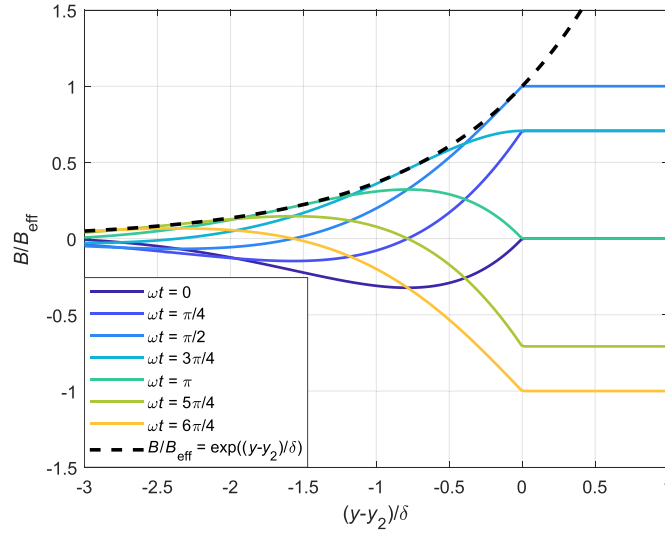
Figure 5. Diffusion of the magnetic field near the surface of the coil (equation (19)).
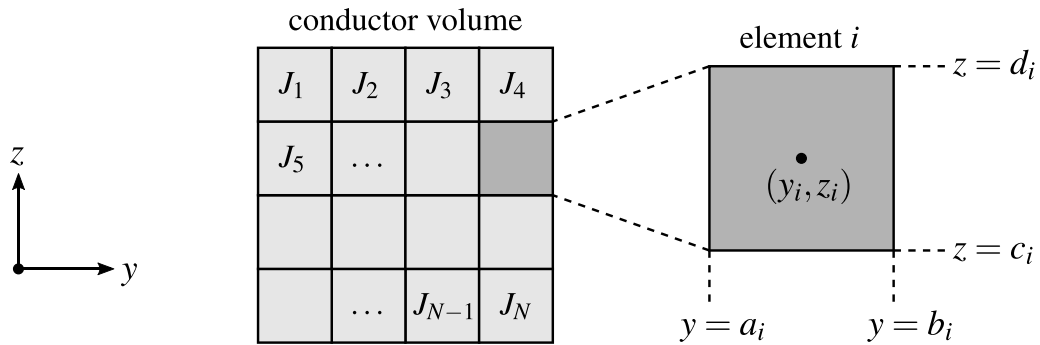

Figure 6. Division of the conductor volume in rectangular elements with uniform current density. This figure shows a cross-sectional plane, to which the current flows perpendicular.

tapes, although the orientation is different. Below, a shortened derivation will be given to enable the reader to make their own implementation.

The conductor cross-section is divided in rectangular elements numbered $i = 1, 2, \ldots, N$, each carrying a uniform current density J_i in the x-direction (see figure 6). The x-component vector potential at the center of each element can be expressed as a linear combination of the element current densities and an external contribution $A_{\text{ext},i}$:

$$A_i = A_{\text{ext},i} + \frac{\mu_0}{2\pi} \sum_{j=1}^{N} K_{ij} J_j. \tag{26}$$

The elements of K are given by [34]:

$$K_{ij} = -\frac{1}{2} \left[\left[uv \left(\ln(u^2 + v^2) - 3 \right) + u^2 \tan^{-1}\left(\frac{v}{u} \right) \right. \right.$$
$$\left. \left. + v^2 \tan^{-1}\left(\frac{u}{v} \right) \right]_{u=y_i-a_j}^{y_i-b_j} \right]_{v=z_i-c_j}^{z_i-d_j}, \tag{27}$$

where element j is bounded by $a_j < y < b_j$, $c_j < z < d_j$ and (y_i, z_i) is a point in the center of element i.

Using the fact that $\partial \mathbf{A}/\partial t = -\mathbf{E} - \nabla\phi$, and assuming $\partial\phi/\partial x = 0$, equation (26) can be rewritten to:

$$\sum_{j=1}^{N} K_{ij} \frac{\partial J_j}{\partial t} = -\frac{2\pi}{\mu_0} \left(E_{x,i} + \frac{\partial A_{\text{ext},i}}{\partial t} \right). \tag{28}$$

This system is solved using Matlab's built-in solver 'ode15s'.

The electric field in the right-hand side is evaluated using the anisotropic continuum model. From equation (6) we have:

$$J_\perp = \sin(\alpha) J_x + \cos(\alpha) J_y. \tag{29}$$

Integration over the height of the coil gives:

$$\int_{-h/2}^{h/2} J_\perp \, dz = \sin(\alpha) \int_{-h/2}^{h/2} J_x \, dz + \cos(\alpha) \int_{-h/2}^{h/2} J_y \, dz. \tag{30}$$

The first term is just $hJ_\perp$ under the assumption of uniform current transfer. The third integral is equal to the applied current $I_a(t)$ divided by the turn length. Therefore the perpendicular current is described by:

Table 1. Conductor properties.

substrate (Hastelloy C276)	63 ± 3	μm
tape width	4 ± 0.13	mm
silver layer *Re*BCO side	2 ± 0.5	μm
silver layer substrate side	1 ± 0.5	μm
copper layer	20 ± 4	μm
solder plating, eutectic InSn	$5 - 10$	μm
average I_c at 77 K	130	A
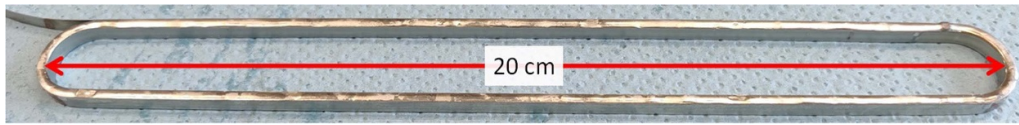
Figure 7. Picture of the soldered coil after removal from the aluminum holder.

$$hJ_\perp = \sin(\alpha) \int_{-h/2}^{h/2} J_x \mathrm{d}z + \cos(\alpha) \frac{I_a}{\ell_{\mathrm{turn}}}. \tag{31}$$

By solving equation (29), J_y can now be expressed in terms of J_x:

$$J_y = \frac{I_a}{h\ell_{\mathrm{turn}}} - \tan(\alpha) \left(J_x - \frac{1}{h} \int_{-h/2}^{h/2} J_x \mathrm{d}z \right). \tag{32}$$

Now that J_y is known, E_x can be computed using equation (8). The continuum model is not limited to the specific numerical method described above. For example, Mataira *et al* successfully implemented it in COMSOL using the *H*-formulation of Maxwell's equations [25, 35].

5. Sample preparation

Two near-identical coils were wound from the same spool of commercial SuperOx *Re*BCO tape (see table 1). An InSn ($T_{\mathrm{melt}} = 118\,°$C) solder-coated tape was used in order to ease the soldering of the turns. The wire was wound onto an aluminum holder with a winding tension of 10 N and the *Re*BCO layer facing the holder. After winding 18.5 turns, the holder was heated to 150 °C in order to melt the solder. During this process, the long legs of the racetrack are compressed in the *y*-direction in order to maintain turn-to-turn contact. Additional flux and solder were applied to the hot coil to fill the space between tapes completely with solder. The coil was then removed from the aluminum holder (figure 7) and placed on an insulating glass-fiber reinforced plastic (GFRP) holder. Finally, copper current terminals were soldered to the coil. The geometrical properties of the coil are listed in table 2.

The coils have an aspect ratio of $2y_2/h = 4.9$. In the high-frequency limit, the magnetic field on the surface is enhanced by a factor 2.87 (see appendix). The corresponding demagnetization factor $N = 0.652$ is used to compute the coupling loss in the high-frequency limit.

Table 2. Geometrical properties of the racetrack coils.

inner radius	y_1	7.5	mm
outer radius	y_2	9.8	mm
tape width/coil height	h	4	mm
turn thickness	d	0.125	mm
number of turns	N	18.5	—
straight section length	ℓ_{straight}	185	mm
mean turn length	ℓ_{turn}	424	mm
tape length	ℓ_{tape}	7.9	m
conductor angle	α	0.295	mrad
inductance	L	72	μH

6. AC loss measurement

6.1. Dipole magnet and sample holder

A NbTi/Cu dipole magnet with a 75 mm × 89 mm rectangular bore is used to apply a uniform and harmonic AC magnetic field to the samples [36]. A special GFRP insert was constructed to mount two racetrack coils in the dipole bore. Here we limit ourselves to the study of coupling loss in an external AC magnetic field. The insert, however, also allows to excite the sample coils with currents up to several hundreds of amperes. These experiments are reported elsewhere. When current is applied to the racetrack coil in the background magnetic field of the dipole, it can generate a torque. By connecting the two coils in anti-series, the overall torque is minimized. This solution simplifies the mechanical design of the insert. In order to transfer the torque between the racetrack coils, the sample holder is fixed inside a thick-walled GFRP tube. This tube also functions as a calorimetric chamber for the AC loss measurement. The current terminals of the coils are connected with common superconducting NbTi/Cu wires in order to minimize the helium boil-off in the chamber.

The self- and mutual inductances of the coils were calculated using a 3D finite-element model in COMSOL, which assumes a uniform current density within the coil volume. The model also takes into account the iron yoke of the dipole magnet. The theoretical self-inductance is 72 μH for each racetrack, and the mutual inductance is more than two orders
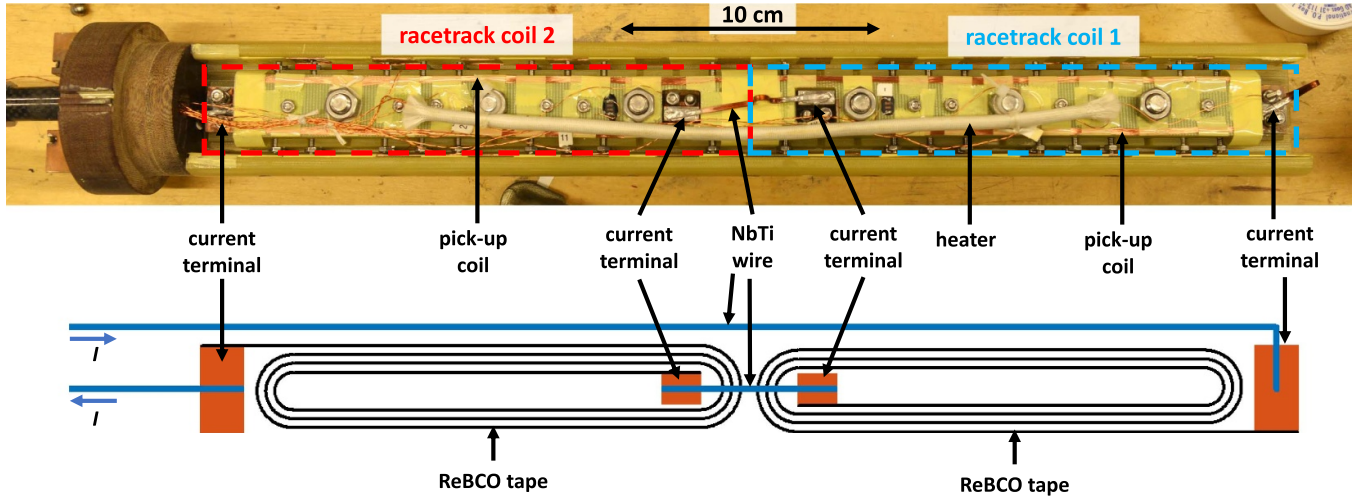
Figure 8. Picture of the sample holder for AC loss measurements with two racetrack coils installed. The no-insulation racetrack coils are located in the GFRP holders underneath the pick-up coils and are connected in anti-series. Racetrack 1 carries a clockwise current while racetrack 2 carries a counter-clockwise current, as illustrated by the sketch (only 3.5 turns out of 18.5 shown).

of magnitude lower. We can thus argue that the inductive coupling between the coils can be neglected.

A picture of the sample holder with the racetrack coils (before insertion into the calorimeter tube) is shown in figure 8. When installed in the dipole magnet, the uniform AC magnetic field is applied perpendicular to the plane of the picture, i.e. parallel to the wide face of the *Re*BCO tapes. The setup allows for simultaneous magnetic and calorimetric determination of the AC loss.

6.2. Magnetic AC measurement using pickup coils

The loss per cycle in a sample exposed to a periodic magnetic field $\mathbf{B}_{\text{ext}}$ can be written as:

$$Q = -\oint \mathbf{B}_{\text{ext}} \cdot \mathbf{dm} = -\int_0^{\frac{2\pi}{\omega}} \mathbf{B}_{\text{ext}} \cdot \dot{\mathbf{m}} \mathrm{d}t. \quad (33)$$

where $\mathbf{m}$ is the magnetic moment of the sample. The principle of the magnetic AC loss measurement is a measurement of $\dot{\mathbf{m}}$ using a set of pick-up coils, in particular the component that is in phase with $\mathbf{B}_{\text{ext}}$.

To enable sensitive measurements, the pick-up coils must be arranged in such a way that the voltage induced by $\dot{\mathbf{B}}_{\text{ext}}$ is minimal. Often this is accomplished by connecting an identical compensation coil (without sample) in anti-series with the pick-up coil of the sample. In our set-up, however, there is not enough space for an empty compensation coil. Therefore, we have opted for a co-axial set of coils as shown in figure 9. The pick-up and compensation coils have an equal turn-area product, and therefore $\dot{\mathbf{B}}_{\text{ext}}$ can be rejected by connecting them in anti-series. Although both coils sense induced currents in the sample, the pick-up coil has more turns, and thus generates a higher voltage. Therefore, the anti-series connection in principle rejects $\dot{\mathbf{B}}_{\text{ext}}$ fully but $\dot{\mathbf{m}}$ only partially.

Below, a quantitative relation between $\dot{\mathbf{m}}$ and the induced pick-up voltage will be derived. Consider an induced current

$\pm I$ flowing in the center of a given winding at $(\pm y_s, z_s = 0)$. The vector potential associated with this current is:

$$A_x(y,z) = \frac{\mu_0 I}{4\pi} g(y,z), \quad (34)$$

where

$$g(y,z) = -\left(\ln((y-y_s)^2 + (z-z_s)^2) - \ln((y+y_s)^2 + (z-z_s)^2) \right). \quad (35)$$

Using the magnetic moment $m_z = 2\ell y_s I$, the unknown current I can be eliminated from equation (34).

$$A_x(y,z) = \frac{\mu_0 m_z}{8\pi\ell y_s} g(y,z). \quad (36)$$

The voltage over a pickup wire at (y_p, z_p) is:

$$V = -\ell \dot{A}_x(y_p, z_p) = -\frac{\mu_0 \dot{m}_z}{8\pi y_s} g(y_p, z_p). \quad (37)$$

By summing over all wires in the pick-up coils total voltage can be found:

$$V = -\frac{\mu_0}{2\pi} k \dot{m}_z \qquad \text{with} \qquad k = \sum_{\text{all wires}} \pm \frac{g(y_p, z_p)}{4 y_s}. \quad (38)$$

The sign of the contributions of the geometrical K is positive or negative depending on whether the pick-up wire is 'directed' in the positive or negative x-direction.

The dimensions of the pick-up and compensation coils are listed in table 3. A 200 mm-long pick-up coil is mounted on each of the two racetrack coils. A single compensation coil of 455 mm length is placed on the outside of the sample holder. The geometric constant k is sensitive to the position of the pick-up wires. Considering a positioning error of ± 0.5 mm, k is in the range of 1860 to 2510 m^{-1}. This uncertainty is
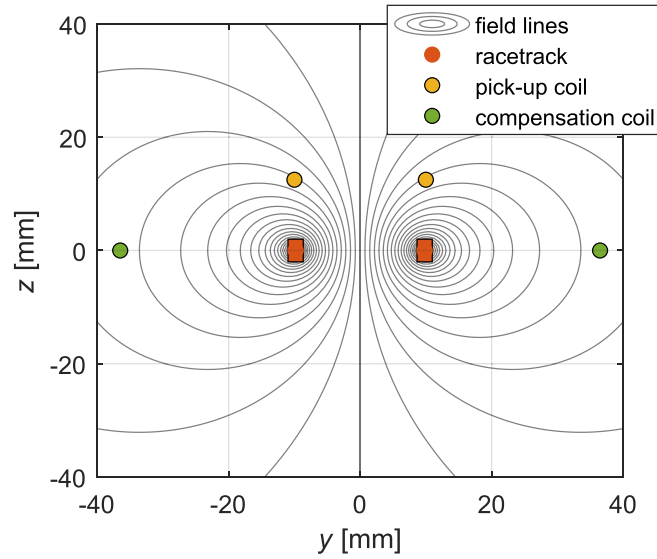
Figure 9. Schematic cross-section showing the position of the racetrack coil legs (the orange rectangles), the pick-up coil (the yellow circles above the racetrack) and the compensation coil (the green circles coplanar with the racetrack). All coils extend in the *x*-direction as shown in figures 2 and 3, perpendicular to the plane shown in the figure. The sketched magnetic field lines are associated with the induced current in the racetrack coil only (i.e. the uniform background field is not shown).

Table 3. Geometry and position of the pick-up and compensation coils.

		pick-up coil	compensation coil
horizontal position	y_p	10 ± 0.5 mm	36.5 ± 0.5 mm
vertical position	z_p	12.5 ± 0.5 mm	0 ± 0.5 mm
no. of turns	N	41	10
length (*x*-direction)	ℓ	200 mm	455 mm

the dominant contribution to the systematic uncertainty in the magnetic AC loss measurement.

By inserting equation (38) into (33) we find the relation between the AC loss and the voltage over the pick-up coils:

$$Q = \frac{2\pi}{\mu_0 k} \int_0^{\frac{2\pi}{\omega}} B_{\text{ext},z}(t) V(t) \mathrm{d}t. \tag{39}$$

Only the component of $V(t)$ with the same frequency and phase as the applied field contributes to the AC loss, so a lock-in amplifier is used to measure it (Stanford Research Systems SR830). At frequencies below 10 mHz, the measurement using the lock-in amplifier becomes prohibitively slow. For these frequencies, the pickup voltage is recorded with a sensitive voltmeter (Keithley 2182a), and equation (39) is evaluated on a computer.

6.3. Calorimetric AC loss measurement

All measurements at 4.2 K are carried out with the sample coils fully submerged in liquid helium. The amount of helium evaporated inside the calorimetric chamber is measured using a mass flow meter (Bronckhorst LOW-ΔP-FLOW). The measurement is calibrated using a resistive heater placed next to the

racetrack coils. The calorimetric measurement thus does not suffer from a relatively large systematic uncertainty such as the one in the magnetic measurement. However, it has a larger noise floor of about ± 10 mW.

7. Results

7.1. Time constant of the coil

In order to find the perpendicular resistivity $\rho_\perp$, the time constant was measured using the 'sudden discharge' method [1]. A current of 40 A is applied until the terminal voltage is stable, and then a switch in series with the coil is opened. The exponential decay of current and magnetic field can be observed in both the terminal and pick-up coil voltage. This test was performed in both liquid nitrogen at 77 K and helium at 4.2 K. At 4.2 K, a background magnetic field of 430 mT was applied to render the InSn solder non-superconducting.

The results of the discharge test are shown in figures 10 and 11. At 77 K, racetrack coil 1 was found to have a time constant of 60 s fitting both coil and pickup voltage. Racetrack coil 2 has slightly higher time constants of 76 s and 73 s, determined by the coil and pickup voltages respectively. At 4.2 K, the time constants are approximately a factor two higher. Again, a somewhat longer time constant is observed in racetrack coil 2.

The time constant is related to the characteristic transverse resistance of the coil through $\tau = L/R_c$, where L is the calculated self-inductance of 72 μH (table 2). The characteristic resistance can be converted into the sought-for perpendicular resistivity as:

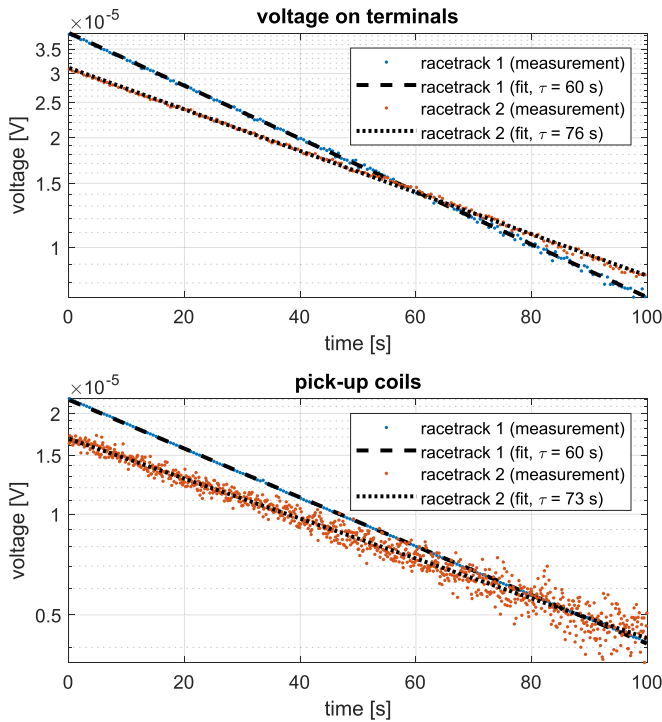$$R_c = \rho_\perp \frac{y_2 - y_1}{h\ell_{\text{turn}}}. \tag{40}$$

Figure 10. Voltage over the racetracks coils (top) and pickup coils (bottom) during a sudden discharge from 40 A at a temperature of 77 K.
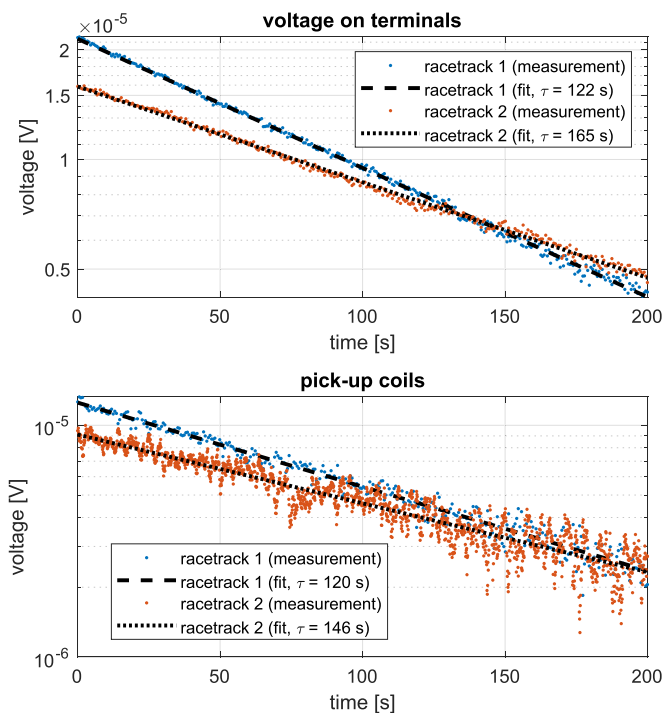

Figure 11. Voltage over the racetracks coils (top) and pickup coils (bottom) during a sudden discharge from 40 A at a temperature of 4.2 K.

Table 4 lists the transverse resistivity values derived from the terminal voltage, which has less noise than the signal from the pick-up coils. These values are used as input for the AC loss calculation.

Table 4. Time constants and transverse resistivities determined from the terminal voltage during a sudden discharge.

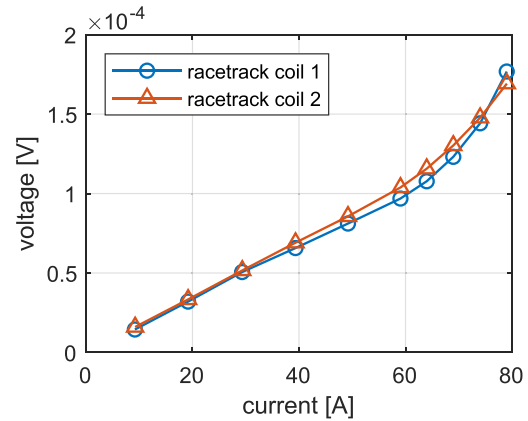| racetrack coil	T (K)	τ (s)	R_c ($\mu\Omega$)	$\rho_\perp$ ($\mu\Omega$m)
1	77	60	1.2	0.89
1	4.2	122	0.59	0.44
2	77	76	0.95	0.70
2	4.2	165	0.44	0.32

Figure 12. *V–I* measurement of racetrack coils 1 and 2 with currents up to 80 A at 77 K.

7.2. Voltage–current and magnetic field measurements

A DC voltage–current measurement was made at 77 K by applying a constant current and waiting at least 5 min (i.e. about five time constants) until the voltage is stable. Figure 12 shows the voltage measured on the current terminals for currents up to 80 A. For currents below 60 A, the voltage increases linear with a slope of 1.7 $\mu\Omega$ due to the resistance of the joints. The voltages rises more steeply above 60 A due to the superconductor transition. It is however difficult to determine an unambiguous value for the critical current because the current path within the coil is unknown during the transition, as confirmed by the magnetic field measured above the coil.

This magnetic field was monitored using a Hall sensor placed 12 mm above the center of the coils (figure 13). Up to 60 A, the field increases linearly with the coil current, with a slope of 260–264 μT/A, confirming the prediction of a finite-element calculation. At higher currents the field saturates, indicating that current is partially bypassing turns that already reached their critical current.

7.3. AC loss measurements at 77 K and 4.2 K

AC loss measurements were performed both at 77 and at 4.2 K. In all measurements a uniform AC field was applied parallel to the surface of the *Re*BCO tapes (figure 13). At 77 K, the NbTi/Cu AC dipole magnet has a high resistance, and only a modest field amplitude of 12 mT can be probed. Although the AC loss in such fields was too small to be detected calorimetrically with this set-up, it could be measured using the pick-up coils.
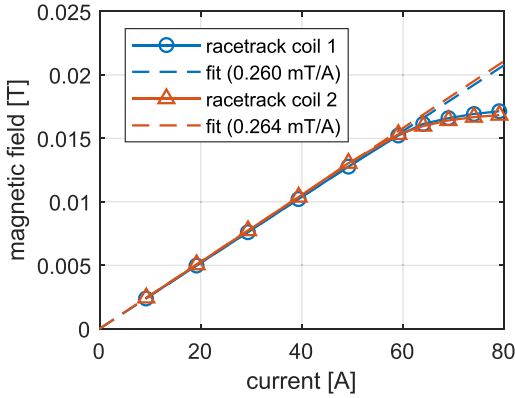
Figure 13. Magnetic field at 12 mm above the racetrack coils measured using a Hall sensor.
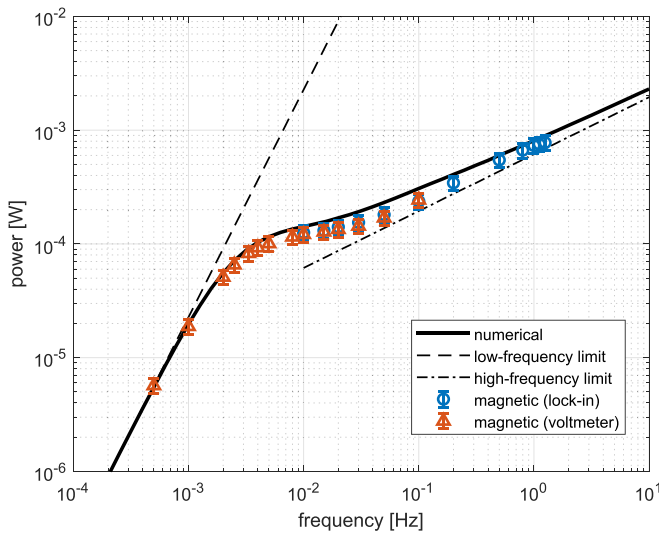

Figure 14. AC loss calculation (lines) and measurement (markers) at $T = 77\,\mathrm{K}$ and $B_0 = 12\,\mathrm{mT}$. The error bars are based on the uncertainty in the geometric constant k (see section 6.2).

By applying a small amplitude magnetic field and aligning it with the tapes, a situation is created in which the coupling loss is large compared to the hysteresis loss. The simulations were done for coupling loss only (i.e. assuming $E_{\mathrm{par}} = 0$).

Figure 14 shows the calculated and measured AC loss powers in a 12 mT sinusoidal magnetic field as a function of frequency. As discussed in section 6.2, the pick-up coil voltage is measured using both a lock-in amplifier and a voltmeter to enable measurement over a large frequency range. The measured data show good agreement between these two methods. The measured AC loss also confirms the frequency characteristic of the model, which predicts the power to be proportional to f^2 at low frequencies and $\sqrt{f}$ at high frequencies. The transition between the two regimes occurs near a characteristic frequency of $1/(2\pi\tau)$, which is 2.7 mHz and 2.1 mHz for coil 1 and 2, respectively. The agreement between the numerical solution and the measured loss is within a factor two for all data. The largest discrepancies between calculation and measurement are observed between 10 mHz and 100 mHz, i.e. somewhat above the characteristic frequencies. The origin
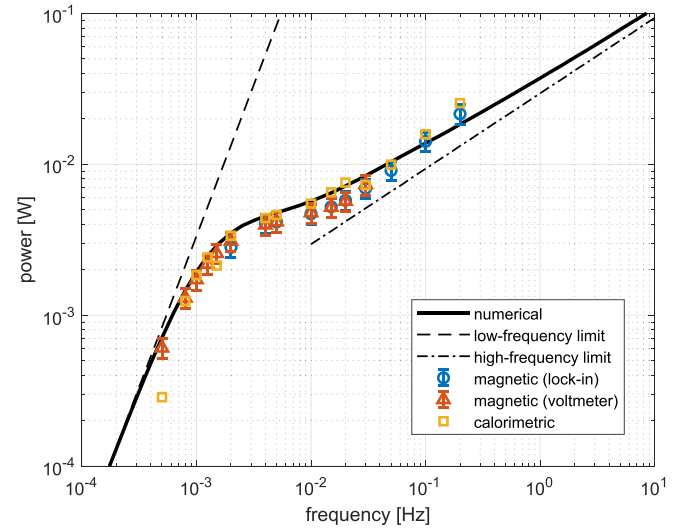

Figure 15. AC loss calculation (lines) and measurement (markers) at $T = 4.2\,\mathrm{K}$ and $B_0 = 100\,\mathrm{mT}$. A 500 mT offset field was applied to rule out superconductivity of InSn.

of this discrepancy is not yet fully understood but may be associated to the simplifications in the model (homogenization and reduction to two dimensions).

At 4.2 K, the dipole magnet is superconducting so that a higher AC magnetic field of 100 mT can be applied. This leads to a ~10–100 times higher loss than at 77 K, enabling a calorimetric measurement. The three measurement methods as well as the model predictions are shown in figure 15. The measurements were performed in a 500 mT DC offset magnetic field to drive the superconducting InSn solder into its normal state. Compared to the measurement at 77 K, the transition between the high- and low-frequency regimes is shifted to about 2 times lower frequencies, as explained by the longer time constants at 4.2 K (122 s and 165 s) and the lower corresponding characteristic frequencies of 1.3 mHz and 1.0 mHz. Once more, the accuracy of the model prediction is fair, agreeing with the data within a factor 2.

A point of discussion is that the loss measurement captures not only coupling loss, but also other contributions such as hysteresis loss, which are neglected in the calculation. Even though hysteresis loss is relatively small in a parallel magnetic field, the model cannot guarantee that it is negligible. However, if hysteresis loss would play a significant role, the measured total loss would exceed the calculated coupling loss. Secondly, one would expect a frequency dependence of $P \propto f$, which is signature for hysteresis. The observed total loss does not show any of these two these characteristics. We can therefore argue that the total loss was dominated by coupling loss.

8. Conclusion

An anisotropic resistivity model with analytical and numerical solutions has been tested to calculate parallel field induced coupling loss in no-insulation *Re*BCO coils. For validation, two small no-insulation racetrack coils were constructed and subjected to AC magnetic field parallel to the surface of the

tape. The AC loss, measured both magnetically and calorimetrically, and entirely dominated by coupling loss, shows reasonable agreement with calculations based on the anisotropic continuum model. The experiment confirmed the predicted frequency characteristic of the coupling loss, which is $P \propto f^2$ at low frequencies and $P \propto \sqrt{f}$ at high frequencies due to the skin effect. The transition between low- and high-frequency regimes was found to occur around a characteristic frequency related to the straightforwardly measured decay time constant by $f_c = 1/2\pi\tau$. The test demonstrated the feasibility of the relatively simple model, which only needs the coil dimension and an easily measured time constant as input.

In a rotating machine or a linear actuator, the coils are subjected to more complicated AC conditions than the ones considered in this work. The armature of a linear actuator, for example, produces a non-uniform magnetic field with higher harmonics. These conditions likely require three-dimensional modeling and more advanced experiments. Nevertheless, the anisotropic continuum seems a feasible approximation for the development of these models.

Data availability statement

All data that support the findings of this study are included within the article (and any supplementary files).

Appendix. Calculation of the effective magnetic field using a conformal map

In this section, the magnetic field on the surface of the coil in the case of perfect shielding ($\delta = 0$) is found using a conformal map. This enhanced magnetic field is then used to estimate the AC loss using the formula for a tall coil in the high-frequency limit. Outside the coil, the current density is zero and therefore $\nabla \times \mathbf{B} = 0$. Since its curl is zero, the magnetic field can be expressed as the gradient of a magnetic scalar potential $\mathbf{B} = -\nabla\phi$. This potential obeys Laplace's equation because $\nabla^2\phi = -\nabla \cdot \mathbf{B} = 0$. Solutions of Laplace's equations have the property that, under a conformal map, they are still solutions of Laplace's equation. We can thus construct the solution in a simple domain and then conformally map it onto the more complicated geometry of the coil. First, the magnetic potential in the *uv*-plane is constructed. The potential can always be written as the real part of a complex potential $\Phi(u,v) = \phi(u,v) + i\psi(u,v)$. For a uniform magnetic field parallel to the *u*-axis, we choose $\phi = u$ so that $-\nabla\phi = \hat{\mathbf{u}}$. To ensure the potential Φ is complex differentiable, it needs to satisfy the Cauchy–Riemann equations:

$$\frac{\partial\phi}{\partial u} = \frac{\partial\psi}{\partial v}, \qquad \frac{\partial\phi}{\partial v} = -\frac{\partial\psi}{\partial u}. \tag{41}$$

This condition is satisfied for a choice of $\psi = v$. The *uv*-plane has to be mapped to the *yz*-plane. To do this, a conformal map $\zeta(w)$ is sought where $\zeta = y + iz$ and $w = u + iv$. The upper half

Table 5. Vertices and angles for the conformal map onto the exterior of a rectangle. The angle δ_j is the counter-clockwise rotation at the corresponding vertex (see figure 16).

vertex	coordinate u_j	angle δ_j
A	∞	2π
B	-1	$\pi/2$
C	$-p$	$-\pi/2$
D	p	$-\pi/2$
E	1	$\pi/2$

of of the *uv*-plane ($u > 0$) is mapped onto the interior of a polygon by the Schwarz–Christoffel mapping [37]:

$$\frac{\mathrm{d}\zeta}{\mathrm{d}w} = \prod_{j=1}^{n} \frac{C_1}{(w - u_j)^{\delta_j/\pi}} \tag{42}$$

where $u_1, u_2, \ldots, u_n$ are the *u*-coordinates corresponding to the vertices of the polygon, δ_j is the angle the transformed axis makes at the vertex in the counter-clockwise direction, and C_1 is a complex number. For a map onto the polygon that overlaps the exterior of the coil in the half plane, the vertices and angles as in table 5 are used. A is a vertex at infinite while B to E correspond to points on the boundary of the rectangle (see figure 16). The number $0 < p < 1$ determines the aspect ratio of the rectangle.

The Schwarz–Christoffel mapping becomes:

$$\begin{aligned}
\frac{\mathrm{d}\zeta}{\mathrm{d}w} &= \frac{C_1}{(w+1)^{1/2}(w+p)^{-1/2}(w-p)^{-1/2}(w-1)^{1/2}} \\
&= C_1\sqrt{\frac{w^2 - p^2}{w^2 - 1}}
\end{aligned} \tag{43}$$

$$\Rightarrow \zeta(w) = C_1\int \sqrt{\frac{w'^2 - p^2}{w'^2 - 1}}\,\mathrm{d}w' + C_2. \tag{44}$$

Here C_2 is a complex integration constant. By means of a substitution $w = \sin(\theta)$ this integral can be expressed as an elliptic integral:

$$\begin{aligned}
\zeta(w) &= C_1\int \sqrt{\frac{\sin^2(\theta) - p^2}{\sin^2(\theta) - 1}}\cos(\theta)\,\mathrm{d}\theta + C_2 \\
&= C_1 p \int \sqrt{1 - p^{-2}\sin^2(\theta)}\,\mathrm{d}\theta + C_2 \\
&= C_1 p\, \mathrm{E}(\sin^{-1}(w)|p^{-2}) + C_2
\end{aligned} \tag{45}$$

where E is the incomplete elliptic integral of the second kind. Figure 16 shows the conformal map for $p = 0.5$ and integration constants $C_1 = 1$, $C_2 = 0$. For this choice of C_1 and C_2, the origin of the *uv*-plane is mapped onto the origin of the *yz*-plane, and the applied magnetic field is in the *y*-direction. By choosing $C_1 = -i$ and $C_2 = y_2$, the line AB lines up with the axis of the coil (*z*-axis). Changing the parameter p results in field around rectangles with different aspect ratios. The magnetic fields for three values of p are shown in figure 17. As seen
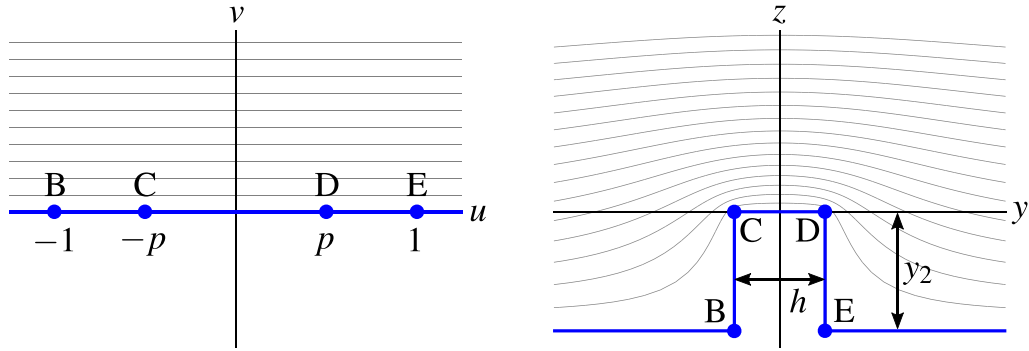
Figure 16. Conformal map of the upper half of the *uv*-plane onto the *yz*-plane with integration constants $C_1 = 1$, $C_2 = 0$. The vertex A is located at infinity. The gray lines are magnetic field lines, which close to BCDE are parallel to that curve.
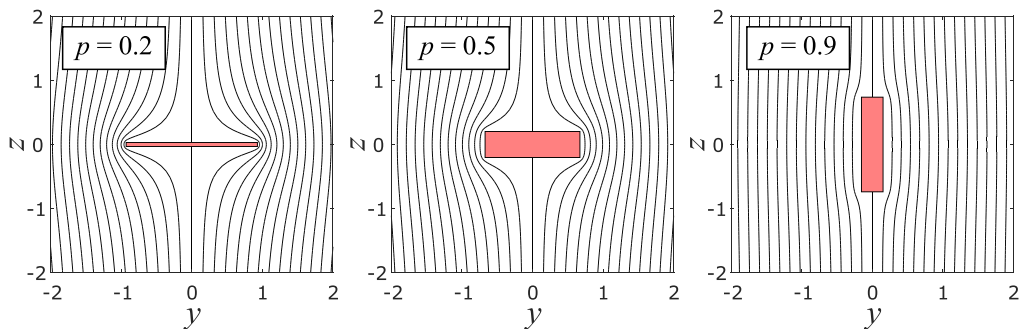

Figure 17. The magnetic field around perfectly shielding rectangles with different aspect ratios. Here, the field for $p = 0.2$, 0.5, 0.9 is shown which results in aspect ratios of $2y_2/h$ of 29.4, 3.31 and 0.207 respectively. The field for $y < 0$ is found using symmetry in the *z*-axis.
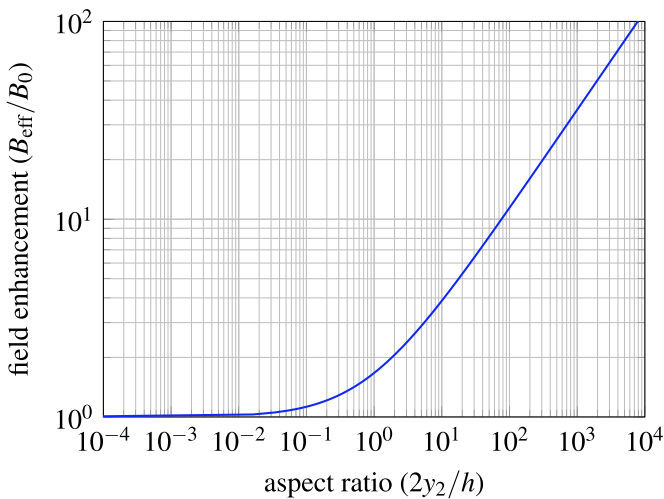

Figure 18. The enhancement of the magnetic field on the surface of the coil as a function of the aspect ratio.

from figure 16, the height of the coil h is equal to twice the real part of point E and the width y_2 is equal to the imaginary part:

$$h = 2C_1 p \Re(\mathrm{E}(p^{-2})) \tag{46}$$

$$y_2 = C_1 p \Im(\mathrm{E}(p^{-2})). \tag{47}$$

Here $\mathrm{E}(p^{-2})$ is the complete elliptic integral given by $\mathrm{E}(p^{-2}) = \mathrm{E}(\pi/2 | p^{-2})$. Therefore the following relation between the aspect ratio of the coil and the parameter p exists:

$$\frac{2y_2}{h} = \frac{\Im(\mathrm{E}(p^{-2}))}{\Re(\mathrm{E}(p^{-2}))} = \tan(\arg(\mathrm{E}(p^{-2}))). \tag{48}$$

To find the average magnetic field on the side of the coil one divides the potential difference between the vertices C and D, which is $\Delta\phi = 2p$, by the distance between those vertices h:

$$B_{\mathrm{eff}} = \frac{\Delta\phi}{h} = \frac{1}{C_1 \Re(\mathrm{E}(p^{-2}))}. \tag{49}$$

From equation (43) it is evident that far away from the coil (large w), the conformal map only distends space by a factor C_1, and thus reduces the magnetic flux density by a factor C_1^{-1}. The enhancement factor for the magnetic field is therefore:

$$\epsilon = \frac{B_{\mathrm{eff}}}{B_0} = \frac{B_{\mathrm{eff}}}{C_1^{-1}} = \frac{1}{\Re(\mathrm{E}(p^{-2}))}. \tag{50}$$

Figure 18 shows the enhancement factor as a function of the aspect ratio. For low aspect ratios (tall coil), the enhancement approaches 1, which means that the magnetic field on the surface is equal to the applied magnetic field B_0. For short coils, the enhancement factor increases approximately with the square root of the the aspect ratio.

ORCID iDs

Simon Otten ⓘ https://orcid.org/0000-0002-1369-6903
Jeroen ter Harmsel ⓘ https://orcid.org/0000-0001-5512-0673
Herman Ten Kate ⓘ https://orcid.org/0000-0001-5597-3190

References

[1] Hahn S, Park D K, Bascunan J and Iwasa Y 2011 HTS pancake coils without turn-to-turn insulation *IEEE Trans. Appl. Supercond.* **21** 1592–5

[2] Yoon S, Kim J, Cheon K, Lee H, Hahn S and Moon S-H 2016 26 T 35 mm all-GdBa$_2$Cu$_3$O$_{7-x}$ multi-width no-insulation superconducting magnet *Supercond. Sci. Technol.* **29** 04LT04

[3] Hahn S *et al* 2019 45.5-Tesla direct-current magnetic field generated with a high-temperature superconducting magnet *Nature* **570** 496–9

[4] Liu J *et al* 2020 World record 32.35 Tesla direct-current magnetic field generated with an all-superconducting magnet *Supercond. Sci. Technol.* **33** 03LT01

[5] Kim Y-G, Hahn S, Kim K L, Kwon O J and Lee H 2012 Investigation of HTS racetrack coil without turn-to-turn insulation for superconducting rotating machines *IEEE Trans. Appl. Supercond.* **22** 5200604

[6] Song J-B, Hahn S, Kim Y, Voccio J, Ling J, Bascuñán J, Lee H and Iwasa Y 2014 Hts wind power generator: electromagnetic force between no-insulation and insulation coils under time-varying conditions *IEEE Trans. Appl. Supercond.* **24** 1–5

[7] Song J-B, Hahn S, Kim Y, Miyagi D, Voccio J, Bascuñán J, Lee H and Iwasa Y 2015 Dynamic response of no-insulation and partial-insulation coils for HTS wind power generator *IEEE Trans. Appl. Supercond.* **25** 1–5

[8] Choi Y, Song J, Yang D, Kim Y, Hahn S and Lee H 2016 A novel no-insulation winding technique of high temperature-superconducting racetrack coil for rotating applications: a progress report in Korea university *Rev. Sci. Instrum.* **87** 104704

[9] Bong U, An S, Voccio J, Kim J, Lee J T, Lee J, Han K J, Lee H and Hahn S 2019 A design study on 40 MW synchronous motor with no-insulation HTS field winding *IEEE Trans. Appl. Supercond.* **29** 1–6

[10] Schreiner F, Liu Y, Zhang Y, Gyuráki R, Noe M and Doppelbauer M 2020 Development of no-insulation racetrack coils wound with 2nd generation HTS tapes for a stator system for wind generators *IEEE Trans. Appl. Supercond.* **30** 1–5

[11] Gao Y *et al* 2020 Design, fabrication and testing of a YBCO racetrack coil for an HTS synchronous motor with HTS flux pump *IEEE Trans. Appl. Supercond.* **30** 1–5

[12] Chae Y S *et al* 2020 Design and analysis of HTS rotor-field coils of a 10-MW-class HTS generator considering various electric insulation techniques *IEEE Trans. Appl. Supercond.* **30** 1–7

[13] Schreiner F, Liu Y and Noe M 2021 Investigation of a six-pole stator system using no-insulation 2nd generation HTS coils for a 10 kW generator demonstrator *IEEE Trans. Appl. Supercond.* **31** 1–5

[14] Wang Y, Weng F, Li J, Šouc J, Gömöry F, Zou S, Zhang M and Yuan W 2020 No-insulation high-temperature superconductor winding technique for electrical aircraft propulsion *IEEE Trans. Transp. Electrification* **6** 1613–24

[15] Dong F, Huang Z, Qiu D, Hao L, Wu W and Jin Z 2019 Design and analysis of a small-scale linear propulsion system for Maglev applications (2)-the HTS no-insulation magnets *IEEE Trans. Appl. Supercond.* **29** 1–5

[16] Dong F, Huang Z, Li X, Hao L, Yao L, Wu W and Jin Z 2019 R&D of no-insulation HTS magnets using 2G wires in a prototype for Maglev applications *IEEE Trans. Appl. Supercond.* **29** 1–5

[17] Lee C-Y, Lee J-H, Lim J, Choi S, Jo J-M, Lee K-S, Chung Y D, Kim S and Lee H 2020 Design and evaluation of prototype high-t_c superconducting linear synchronous motor for high-speed transportation *IEEE Trans. Appl. Supercond.* **30** 1–5

[18] Wang Y 2020 AC losses of no-insulation high temperature superconductor (RE)Ba$_2$Cu$_3$O$_x$ coils induced by ripple magnetic fields in machines (https://doi.org/10.36227/techrxiv.12611825.v1)

[19] Hwang Y, Ahn M, Lee T, Lee W and Ko T 2013 Experimental study of the effects of alternating fields on HTS coils according to the winding insulation conditions *Supercond. Sci. Technol.* **26** 085021

[20] Hahn S, Kim Y, Ling J, Voccio J, Park D K, Bascuñán J, Shin H-J, Lee H and Iwasa Y 2013 No-insulation coil under time-varying condition: magnetic coupling with external coil *IEEE Trans. Appl. Supercond.* **23** 4601705

[21] Lee J, Lee T S, Kwon O J, Lee H and Ko T K 2014 Experimental study on low-pass filtering characteristic of axial magnetic field of no-insulation and partial-insulation HTS coils carrying a DC-biased AC current *IEEE Trans. Appl. Supercond.* **24** 1–5

[22] Lee W S, Park Y G, Kim J, Song S, Jeon H, Kim Y-G, Lee H and Ko T K 2016 Magnetic field stability analysis on no-insulation and turn-to-turn soldered HTS magnets under sinusoidal noise operation *IEEE Trans. Appl. Supercond.* **26** 1–5

[23] Choi Y, Yang D, Kim Y, Kim S, Song J and Lee H 2016 A study of the electromagnetic characteristics of no-insulation GdBCO racetrack coils under an external magnetic ripple field *Supercond. Sci. Technol.* **29** 045010

[24] Kim J, Nam S, Jeon H, Kim J, Jang J Y and Ko T K 2016 Experimental analysis on AC loss and fault current test of HTS coils co-wound with various inserted materials *IEEE Trans. Appl. Supercond.* **26** 1–5

[25] Mataira R, Ainslie M, Badcock R and Bumby C 2020 Finite-element modelling of no-insulation HTS coils using rotated anisotropic resistivity *Supercond. Sci. Technol.* **33** 08LT01

[26] Otten S, Kario A, Demenčik E, Nast R and Grilli F 2020 Anisotropic monoblock model for computing AC loss in partially coupled Roebel cables *Supercond. Sci. Technol.* **33** 094013

[27] Gao P *et al* 2019 Inter-strand resistance and ac loss in resin-filler impregnated ReBCO Roebel cables *Supercond. Sci. Technol.* **32** 125002

[28] Coey J 2010 *Magnetism and Magnetic Materials* (Cambridge: Cambridge University Press)

[29] Navau C, Cardoso C, de Lima O and Araujo-Moreira F 2004 Experimental and theoretical study of demagnetization fields in superconducting samples of orthorhombic shape *J. Appl. Phys.* **96** 486–92

[30] Pugh B, Kramer D and Chen C 2011 Demagnetizing factors for various geometries precisely determined using 3-D electromagnetic field simulation *IEEE Trans. Magn.* **47** 4100–3

[31] Prozorov R and Kogan V 2018 Effective demagnetizing factors of diamagnetic samples of various shapes *Phys. Rev. Appl.* **10** 014030

[32] Brandt E H 1994 Thin superconductors in a perpendicular magnetic AC field: general formulation and strip geometry *Phys. Rev.* B **49** 9024–40

[33] Brandt E H 1996 Superconductors of finite thickness in a perpendicular magnetic field: strips and slabs *Phys. Rev.* B **54** 4246–64

[34] Otten S and Grilli F 2019 Simple and fast method for computing induced currents in superconductors using freely available solvers for ordinary differential equations *IEEE Trans. Appl. Supercond.* **29** 8202008

[35] Mataira R, Ainslie M D, Badcock R and Bumby C W 2021 Modelling parallel-connected, no-insulation high-t_c superconducting magnets *IEEE Trans. Appl. Supercond.* **31** 1–5

[36] Daum C, Geerinck J, Heller R, Schmuser P and Bracke P 1988 Superconducting correction magnets for the HERA proton storage ring *IEEE Trans. Magn.* **24** 1377–80

[37] Schinzinger R and Laura P A 1991 *Conformal Mapping: Methods and Applications* (Amsterdam: Elsevier)